

Supporting information for

Silver-induced reconstruction of an adeninate-based metal-organic framework for encapsulation of luminescent adenine-stabilized silver clusters

Dries Jonckheere^a, Eduardo Coutino-Gonzalez^b, Wouter Baekelant^b, Bart Bueken^a, Helge Reinsch^{a,c}, Oliver Fenwick^{d,e}, Fanny Richard^e, Paolo Samorì^e, Rob Ameloot^a, Johan Hofkens^b, Maarten B. J. Roeffaers^{a*}, Dirk E. De Vos^{a*}

^a KU Leuven, Leuven Chem&Tech: Centre for Surface Chemistry and Catalysis (COK), *Celestijnenlaan 200F post box 2461, 3001 Leuven, Belgium*

^b KU Leuven, Leuven Chem&Tech: Molecular Imaging and Photonics (MIP), *Celestijnenlaan 200F post box 2404, 3001 Leuven, Belgium*

^c Christian-Albrechts-Universität zu Kiel, Institut für Anorganische Chemie, *Max-Eyth-Straße 2, 24118 Kiel, Germany*

^d Queen Mary University of London, *School of Engineering and Materials Science, Mile End Road, London E1 4NS, UK*

^e ISIS & icFRC, Université de Strasbourg & CNRS, *8 allée Gaspard Monge; 67000 Strasbourg, France*

1. Used chemicals and techniques

1.1 Chemicals used

Silver nitrate (99.85%), adenine (99%), *N,N*-dimethylformamide (> 99%), formic acid (98%+) and zinc acetate dihydrate (>98%) were purchased from Acros, ethanol (pure), methanol (Laboratory reagent grade), hydrochloric acid (37% solution), sodium hydroxide (analytical grade) and glacial acetic acid (>99.7%) from Fisher Scientific, dimethyl 4,4'-biphenyldicarboxylate (4,4'-BPDA) (>98%), 4,4'-*trans*-stilbenedicarboxylic acid (4,4'-*trans*-SBDA) (> 90%), terephthalic acid (>99%) and trifluoroacetic acid (>99.0%) from TCI Chemicals, trimesic acid (95%) from Aldrich, aluminium nitrate nonahydrate (>98%) from Sigma-Aldrich, nitric acid (65% solution) from ChemLab, zirconium chloride (sublimed, 99.95%), zirconyl chloride octahydrate (98%) and aluminium chloride hexahydrate (99%) from ABCR. All chemicals were used as received without any further purification steps.

One of the linkers for the synthesis of bio-MOF-1 and MIL-140C was synthesized in-house from its dimethyl ester. Hereto, dimethyl 4,4'-biphenyldicarboxylate (5 g) and NaOH (15 equivalents) were dissolved in 600 mL deionized water with heating to 100°C for 6 h. After cooling down, the clear solution was filtered using vacuum filtration to remove any unreacted dimethyl ester. Subsequently, the clear solution was further cooled down with an ice bath to 15°C and the *pH* was adjusted to 1 with hydrochloric acid, yielding the precipitation 4,4'-biphenyldicarboxylic acid as a white solid. Finally, the dicarboxylic acid was recovered by vacuum filtration and dried at 60°C overnight. Typical yields of 80 – 90% are observed.

1.2 Synthesis of screened MOFs

All materials for the initial screening were synthesized according to literature procedures: UiO-66¹, MOF-808², MIL-140C³, MIL-53(Al)⁴, MIL-68(Al)⁵ modulated with 3.33 equivalents of trifluoroacetic acid, MIL-96(Al)⁶ and ZIF-8⁷. All products were washed three times with the corresponding fresh solvents used for synthesis, followed by three washing steps with ethanol to remove unreacted metal salts and linkers. All chemicals were obtained commercially and used without further purification.

bio-MOF-1 was synthesized following the procedure described by An *et al.*⁸ Prior to material synthesis, 4,4'-biphenyldicarboxylic acid (4,4'-BPDA) was synthesized from its dimethyl ester, see section SI 1.1. For bio-MOF-1 synthesis, adenine (0.625 mmol) and in-house 4,4'-biphenyldicarboxylic acid (1.25 mmol) were dissolved in 67.5 ml of DMF (*N,N*-dimethylformamide) in a glass Schott pressure-plus synthesis bottle. Upon addition of an aqueous solution of zinc acetate dihydrate (1.875 mmol) in 10 mL of deionized water, a white precipitate was formed. This first precipitate was dissolved again upon addition of 695 μ L of a 65% solution of nitric acid (5 mmol). The resulting transparent solution was put in an oven for 24 h at 130°C without stirring. A similar synthesis procedure was applied for an analogous material containing 4,4'-*trans*-stilbenedicarboxylic acid (4,4'-*trans*-SBDA), known as ZJU-48.⁹ The resulting powders were recovered by vacuum filtration, suspended five times in 50 mL of fresh *N,N*-dimethylformamide (DMF) to remove unreacted metal salts and linkers, before being air dried for 6 h at room temperature and finally overnight at 80°C.

1.3 Silver loading experiments

For a typical silver loading experiment, 250 mg of MOF was added to a 10 mL solution of 69.5 mg AgNO₃ (40 mM) in various solvent ratios of ethanol and water, based on a reported¹⁰ 5-1 ratio from literature. Because of the presence of a mildly reducing alcohol, these solutions have the intrinsic property to reduce silver ions. The suspensions were agitated overnight (16 h) at 350 rpm and the powders were collected using vacuum filtration. Subsequently, the powders were air-dried while stored in darkness to avoid light-induced reduction of silver ions during drying and storage. For bio-MOF-1 various EtOH-H₂O ratios were tested to find the optimal reduction conditions. All chemicals were used without further purification.

Table S. 1: Overview of EtOH-H₂O mixtures used for silver-induced transformation of bio-MOF-1 to MOF-69A

EtOH-H ₂ O	EtOH (mL)	H ₂ O (mL)	EtOH-H ₂ O	EtOH (mL)	H ₂ O (mL)
EtOH	10	0	1-1	5	5
9-1	9	1	1-2	3.34	6.66
7-1	8.75	1.25	1-4	2	8
5-1	8.34	1.66	1-7	1.25	8.75
4-1	8	2	H ₂ O	0	10
2-1	6.66	3.34			

1.4 Structural and physicochemical characterization

Powder X-ray diffraction (PXRD) patterns were recorded on a STOE STADI MP in Bragg-Brentano mode (2 θ - θ geometry; CuK $_{\alpha 1}$, 1.54060 Å) using a linear position sensitive detector to confirm the crystallinity and structure of all synthesized materials. Pawley refinement was performed with TOPAS software.

Liquid phase ¹H NMR spectra were recorded on a Bruker Avance 400 MHz spectrometer equipped with a BBI 5 mm probe. Signal due to the presence of water were suppressed by applying an adapted pulse program: p1 8 μ s; pl1 -1 db; pl9 50 db; o1P on the resonance signal of water, determined from a previous ¹H-NMR measurement: ds 2; ns 32; d1 5s; aq 2.55 s; sw 16. Prior to the NMR measurements, 1 mg of powder sample was digested in 700 μ L DMSO-d₆ with 30 μ L of a 40% solution of HF in water.

Fourier transform infrared spectroscopy (FTIR) measurements were performed on a Bruker IFS 66v/S spectrometer. Thin transparent wafers of KBr mixed with 1 wt% of sample were prepared and dried at 60°C and 80°C.

Scanning electron microscopy (SEM) micrographs were recorded using a JEOL-6010LV SEM after depositing a palladium/gold layer on the samples using a JEOL JFC-1300 autofine coater under Ar plasma.

Nitrogen physisorption measurements were performed on a Micromeritics 3Flex surface analyser at 77 K after sample activation under vacuum at 373K for 4 h.

Thermogravimetric analysis (TGA) of the samples was performed using a TA Instruments Q500 thermogravimetric analyser. The samples were treated under an oxygen flow with a linear heating ramp of 10°C/min to 650 °C. TA Universal Analysis software was used for post-measurement data handling.

Inductively coupled plasma (ICP) was performed to determine the metal contents of the powders using an Agilent ICP-MS 7700X. 50 mg of the MOF powders was digested in a mixture of 0.5 mL 65% HNO₃ and 3 mL solution of 40% HF in water.

X-ray Photoelectron Spectroscopy (XPS) was additionally performed to probe differences in metal content at the outer surface compared to the bulk of the material for selected powders. The instrument used was a Thermo Scientific™ K-Alpha™ X-ray Photoelectron Spectrometer (XPS) System with an Al_{Kα} source producing x-rays with energy $h\nu = 1486.7 \text{ eV}$ that are focussed to a 200 x 200 μm² spot. An electron flood gun was applied during the XPS measurements to minimize charging effects.

Photoelectron spectroscopy in air (PESA) was used to measure the ionization potentials of the MOF powders using a Riken Keiki spectrophotometer (Japan) model AC-2. The conditions employed during the measurements were a scanning energy range from 4.4 to 6.2 eV with a measurement interval of 0.05 eV, an integration time of 10 s and UV power of 600 nW.

1.5 Optical characterisation

The silver-loaded MOFs and the pristine MOF materials were subjected to an additional fluorescence characterization. For this purpose, the powders were loaded in quartz cuvettes (Hellma) with a path length of 1 mm and sealed by a Teflon stopper.

Emission spectra were measured using a FLS 920 fluorescence spectrophotometer (Edinburgh Instruments, Photonics division) at different excitation wavelengths from 250 to 600 nm with 5 nm intervals. For each excitation wavelength, the emission (280-800 nm) was collected starting 30 nm above the excitation wavelength. For UV excitation, the emission signal above 405 nm was measured using a 400 nm long pass glass filter to avoid second order excitation interference and the collected signal was corrected for the transmittance of this filter. These emission spectra were compiled in a Matlab-environment to two-dimensional emission-excitation profiles, where the raw data were interpolated to a 1 nm x 1 nm resolution and corrected for noise and background.

The UV-VIS absorption properties of the pristine MOF and Ag-loaded MOFs were determined with Diffuse Reflectance Spectroscopy (DRS), using a Lambda 950 UV-VIS spectrophotometer (PerkinElmer). BaSO₄ powder was used as a reference in the wavelength range of 200 to 800 nm.

Quantum yields (QY) of the powders were measured according to a previous literature report¹¹ using a Horiba Jobin Yvon fluorolog FL 33-22 fluorimeter coupled with a Labsphere optical Spectralon coated integrating sphere (100 mm diameter), with high reflectance in the UV-VIS and NIR region. The sphere accessories were made from Teflon or Spectralon. Excitation was provided by a xenon lamp with a monochromator. Emitted fluorescence was collected at a right angle to the excitation and sent through the side port of the sphere to a second monochromator coupled to a photon multiplier tube (PMT). In the sphere, a baffle between the sample holder and the detection port was placed to avoid direct observation of the scattered light and the fluorescence from the sample. Scattering and emission spectra were recorded for the empty sphere, as well as for the sample in the beam and out of the beam to take into account re-absorption of scattered excitation light. Long-pass filters were used when appropriate to

avoid second-order effects. As a reference, the quantum yield of a commercial blue phosphor, BaMgAl₁₀O₁₇:Eu²⁺ (BAM), was also measured and verified to be in line with literature values (≈95 %).

The fluorescence decay times were determined by time-correlated single photon counting (TCSPC) measurements; the setup has been described in detail previously.¹² Briefly, the frequency-doubled output (375 nm, 8.18 MHz, 2 ps FWHM) of a mode-locked Ti:sapphire laser (Tsunami, Spectra Physics) was used as excitation source. The linearly polarized excitation light was rotated to a vertical direction by the use of a Berek compensator (New Focus) in combination with a polarization filter and directed onto the sample. The sample was mounted at an angle of 55° with respect to the incident light. The emission was collected under 90° with respect to the incident light and guided through a polarization filter that was set at the magic angle (54.7°) with respect to the polarization of the excitation beam. The fluorescence was spectrally resolved by a monochromator (Sciencetech 9030, 6-mm bandwidth), and detected by a microchannel plate photomultiplier tube (MCP-PMT, R3809U, Hamamatsu). A time-correlated single photon timing PC module (SPC 830, Becker & Hickl) was used to obtain the fluorescence decay histogram in 4096 channels. The decays were recorded with 10000 counts in the peak channel, in time windows of 25 ns corresponding to 6.1 ps/channel and analysed globally with a time-resolved fluorescence analysis (TRFA) software. The full width at half-maximum (FWHM) of the IRF was typically in the order of 32 ps. The quality of the fits was judged by the fit parameters χ^2 (< 1.2), $Z\chi^2$ (< 3) and the Durbin Watson parameter (1.8<DW<2.2) as well as by the visual inspection of the residuals and autocorrelation function.¹³ The fluorescent decays were analysed first individually in terms of decay times and their associated pre-exponential factors. These measurements were performed according to previous reports on luminescent silver clusters in zeolites.¹⁴

Fluorescence microscopy images were recorded on a fully automated inverted *confocal* microscope (Olympus IX81). The luminescence after excitation with a 370 nm laser was detected with a photomultiplier tube (PMT) and the image was reconstructed with software (FV10-ASW 3.0). A dichroic mirror directs the excitation laser light through the objective lens (Olympus, 100x, oil immersion, NA: 1.40) onto the sample. The luminescence is captured by the same objective lens, after which it passes through a pinhole into multiple detectors, which are spectrally cleaned up using bandpass and longpass filters. All obtained images were analysed and false-coloured using ImageJ (v1.47g). There is also the possibility to obtain transmission images. *Wide-field* fluorescence images were collected through the eyepieces of the same setup using an adapter from Micro-Tech-Lab (Austria) to connect a Canon EOS5D colour camera to the eyepiece and a mercury lamp for UV excitation light.

2. Structure bio-MOF-1 and ZJU-48

The structural build-up of the bio-MOF-1⁸ and ZJU-48⁹ frameworks is given in Figure S1. Zinc-adeninate clusters (Fig. S.1a), consisting of one adenine molecule and two to two equivalent Zn²⁺ ions, are formed and interconnect via one μ_4 -connected oxygen atom to a pillar of zinc adeninate clusters (Fig. S.1b). The coordination mode of adeninate is in such a way that all pyrimidine and imidazole nitrogen atoms of adenine are coordinated to zinc, leaving a free $-\text{NH}_2$ group. These pillars are interconnected with dicarboxylates to form one-dimensional pores (Fig. S.1c) with a diameter of about 1 nanometre. From Figure S.1c it is also clear that the zinc-adeninate clusters are connected differently in ZJU-48 because of the longer length of the dicarboxylate, which also causes the zinc-adeninate clusters and crystal faces to be spatially more separated. The major difference is that bio-MOF-1 is an anionic framework, yielding cation exchange capacity of dimethyl ammonium (DMA^+) cations⁸, while ZJU-48 is reported to be cationic⁹.

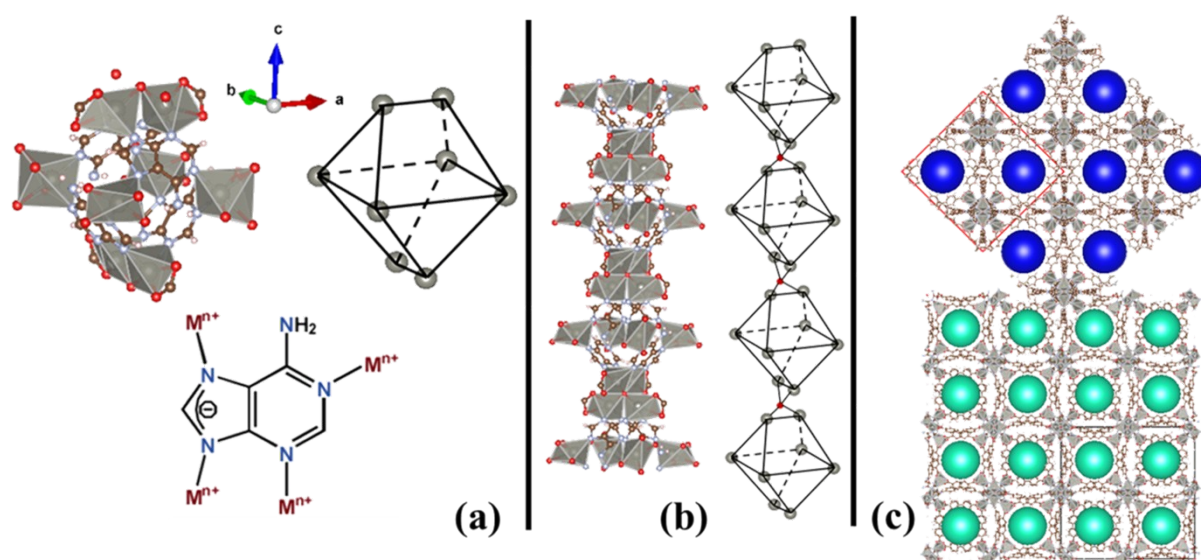


Figure S.1: Structure of bio-MOF-1 and ZJU-48: (a) zinc-adeninate cluster and adeninate coordination, (b) zinc-adeninate pillar, (c) visualization along the unidimensional pore for bio-MOF-1 (turquoise) and ZJU-48 (dark blue).

3. Silver-induced structural transformation of ZJU-48

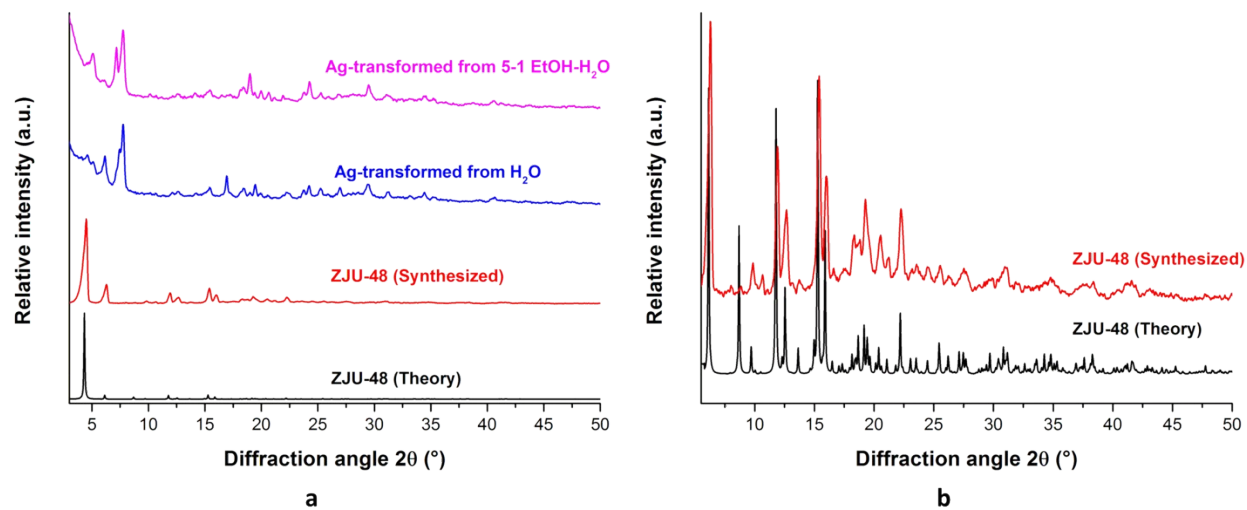


Figure S.2: (a) Solvent influence on the silver induced transformation of ZJU-48 and (b) detailed PXRD pattern beyond the first reflection at $4^\circ 2\theta$ to prove the correct synthesis of ZJU-48. The PXRD reflection in panel (a) at $8.33^\circ 2\theta$ is comparable to what is observed for the gel precipitate obtained by mixing silver nitrate and adenine in a 1-1 ratio.

4. Structural transformation of bio-MOF-1 using various Ag-adenine ratios

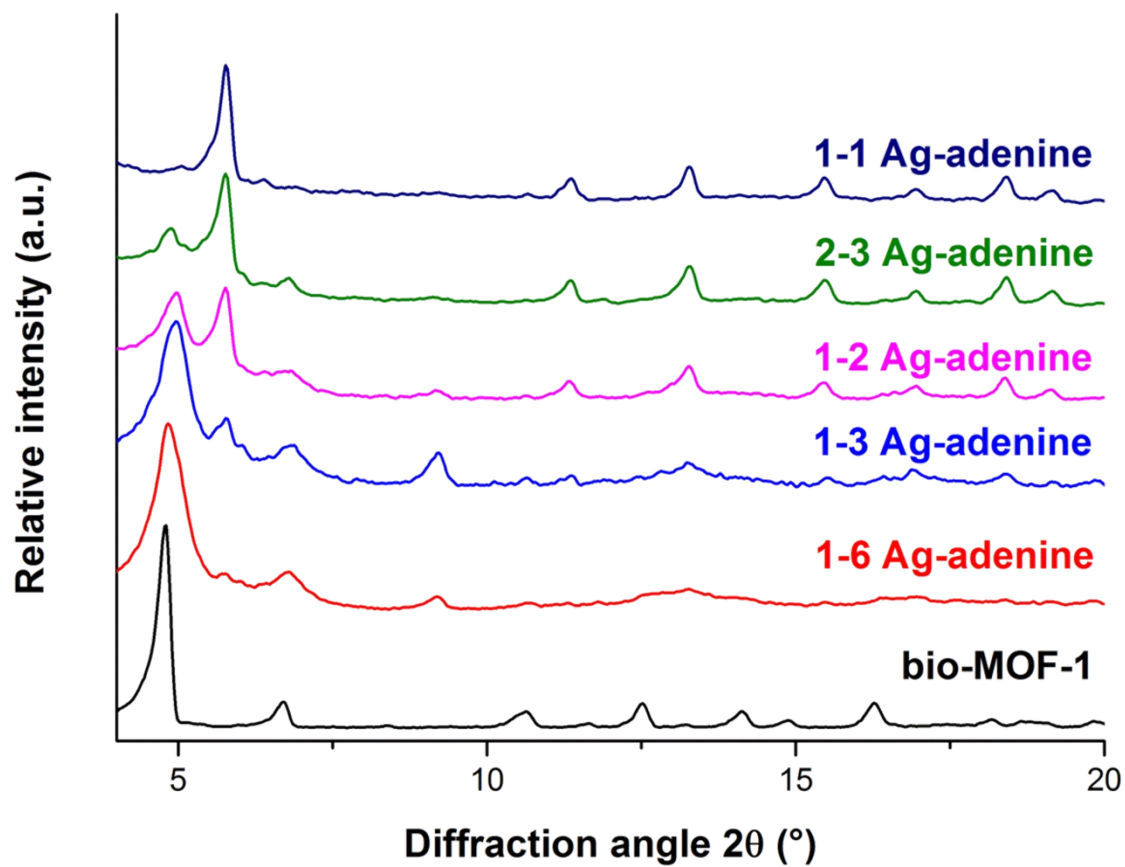


Figure S.3: Influence of the ratio of Ag⁺ in solution to adenine in bio-MOF-1 on the transformation of bio-MOF-1

5. Influence of solvent on bio-MOF-1 transformation to MOF-69A

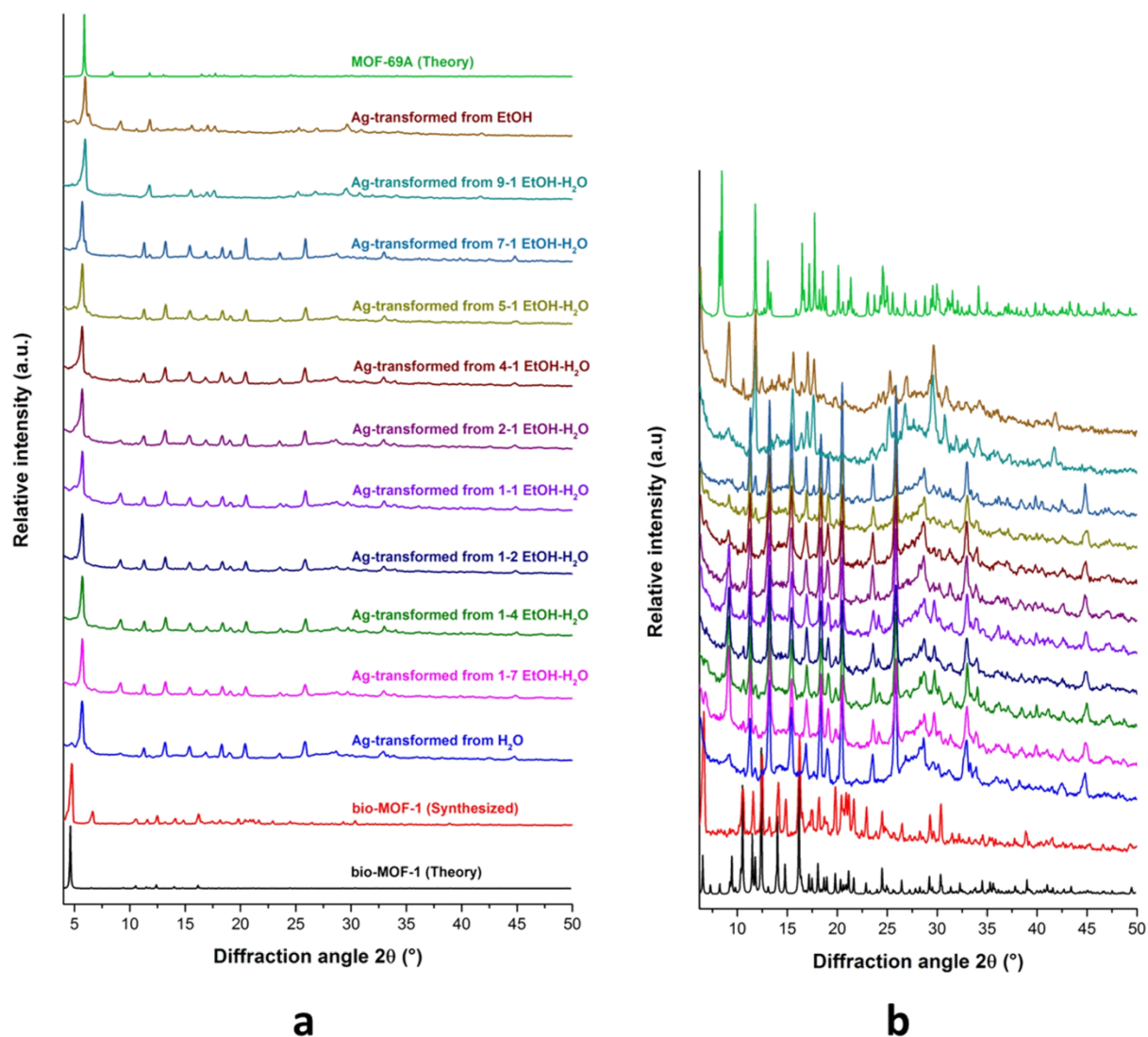
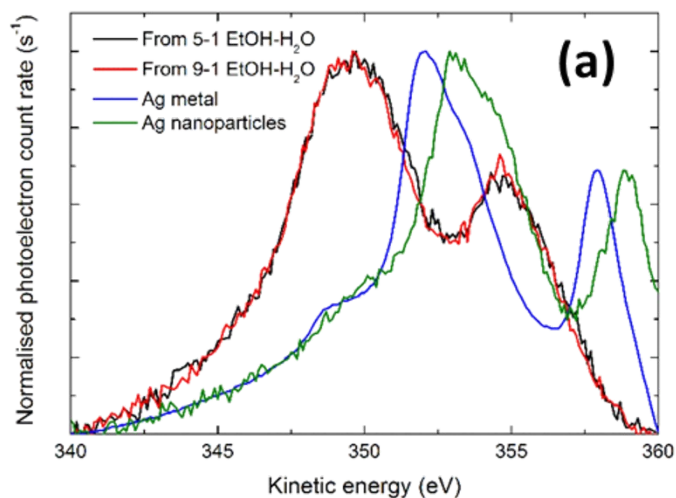


Figure S.4: (a) Solvent influence on the silver induced transformation of bio-MOF-1 to MOF-69A; (b) Detail of PXRD diffractograms shown in (a) beyond the first reflection ($2\theta > 7^\circ$).

6. XPS Auger spectra



(b)

Material	Modified Auger parameter
From 5-1 EtOH-H ₂ O	723.4
From 9-1 EtOH-H ₂ O	723.3
Ag metal	726.0
Ag nanoparticles	726.0

Figure S. 5 (a) Silver Auger spectra recorded by XPS of Ag-transformed bio-MOF-1 samples (at two EtOH-H₂O selected ratios) with analogous spectra for silver metal and silver nanoparticles (10 nm diameter, sodium citrate stabilized, Sigma Aldrich). (b) Table of the modified Auger parameters for silver in these materials. The modified Auger parameters (MAP) are equal in this case to the sum of the binding energy of 3d_{5/2} electrons and the kinetic energy of M₄N_{4,5}N_{4,5} Auger electrons and quantify the shift of atomic orbitals due to their chemical environment but without susceptibility to charging effects during the measurement.

7. FT-IR study on silver-induced ZJU-48 framework transformation

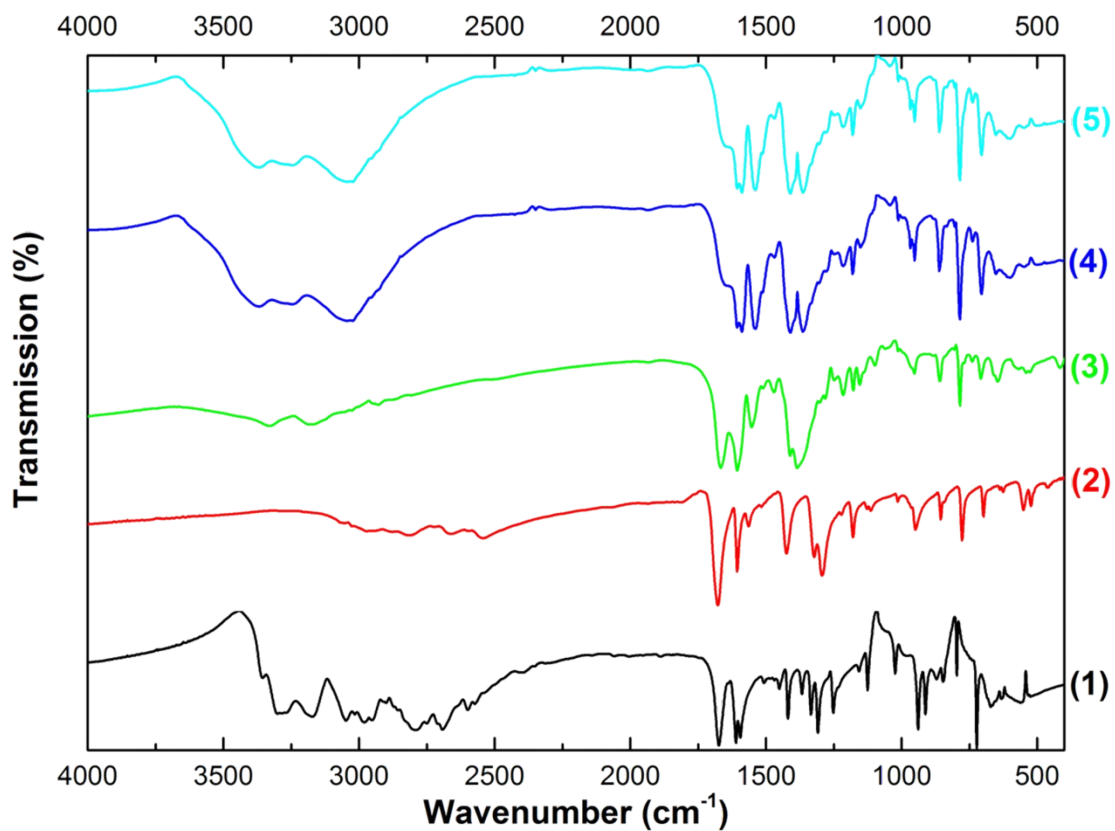


Figure S.6: FT-IR study of silver exposure of ZJU-48: (1) adenine, (2) 4,4'-*trans*-SBDA, (3) ZJU-48, (4) ZJU-48 after exposure to Ag⁺ in H₂O, (5) ZJU-48 after exposure to Ag⁺ in 5-1 EtOH-H₂O.

8. Thermogravimetric analysis on silver-transformed bio-MOF-1 and ZJU-48

Thermogravimetric analysis (TGA) of bio-MOF-1 and silver-transformed samples (Figure S.6 left) shows that the formed structure upon loading of bio-MOF-1 with silver has a different thermal behaviour compared to pristine bio-MOF-1. The weight losses in bio-MOF-1 are, according to literature, attributable to the loss of physisorbed DMF and water (30-200°C), DMA⁺ cations (200-300°C) followed by structural breakdown of first 4,4'-BPDA (m.p. above 300°C) and then adenine (m.p. 360-365°C). Since adenine is bound very tightly in the zinc-adeninate pillars, the decomposition of adenine occurs at higher temperatures and is spread out over a wider range, even up to 500°C, when compared to free adenine (360°C). The thermal decomposition is more gradual for bio-MOF-1 (300-450°C) due to the two linkers that decompose at different temperatures (see also the first derivative signal in Figure S.6 bottom left). In contrast, the silver-transformed samples have very sharp thermal decomposition behaviour at 370°C. In this case, the thermal behaviour is dominated by seemingly only one of the original linkers in bio-MOF-1. Here it is possible that both linkers degrade simultaneously because of the embedded silver acting as an oxidation catalyst or because of different, weaker linker binding modes in the less thermally stable MOF-69A.

For ZJU-48 the same occurs: in the as-synthesized material gradually first physisorbed and chemisorbed solvent molecules are lost, followed by a gradual framework destruction by loss of the 4,4'-*trans*-SBDA linker (400°C) and the adenine linker (480°C), see figure S.6, bottom. As for bio-MOF-1, upon silver loading the thermal destruction of the sample is observed as a sharp single step, caused by a catalytic oxidation effect of the embedded silver.

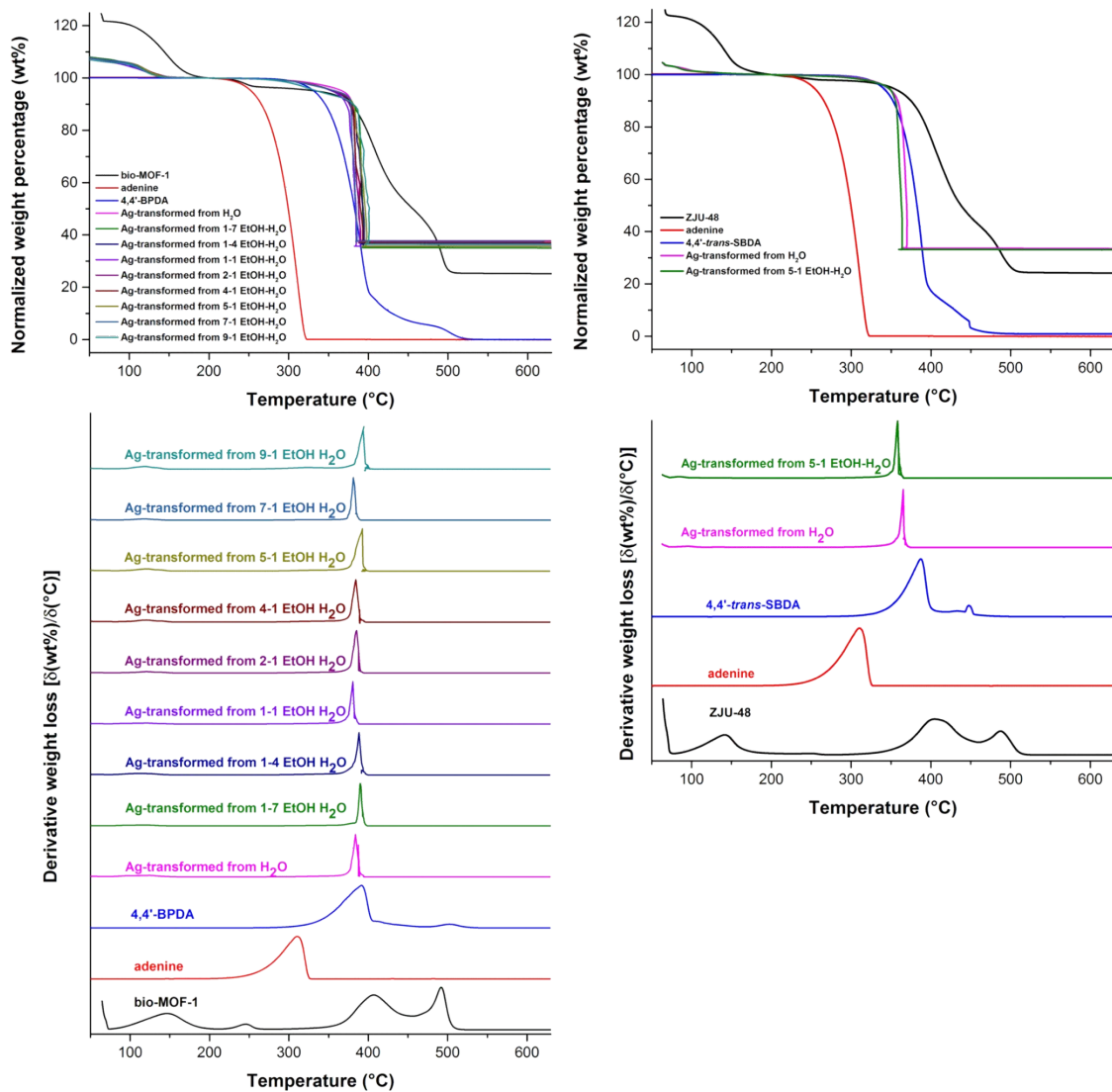


Figure S.7: Normalized thermogravimetric signals (top) and the first derivative of the signal (bottom) for bio-MOF-1 and derived samples (left and) and ZJU-48 and derived samples (right).

9. SEM pictures of bio-MOF-1 and ZJU-48, before and after exposure to silver

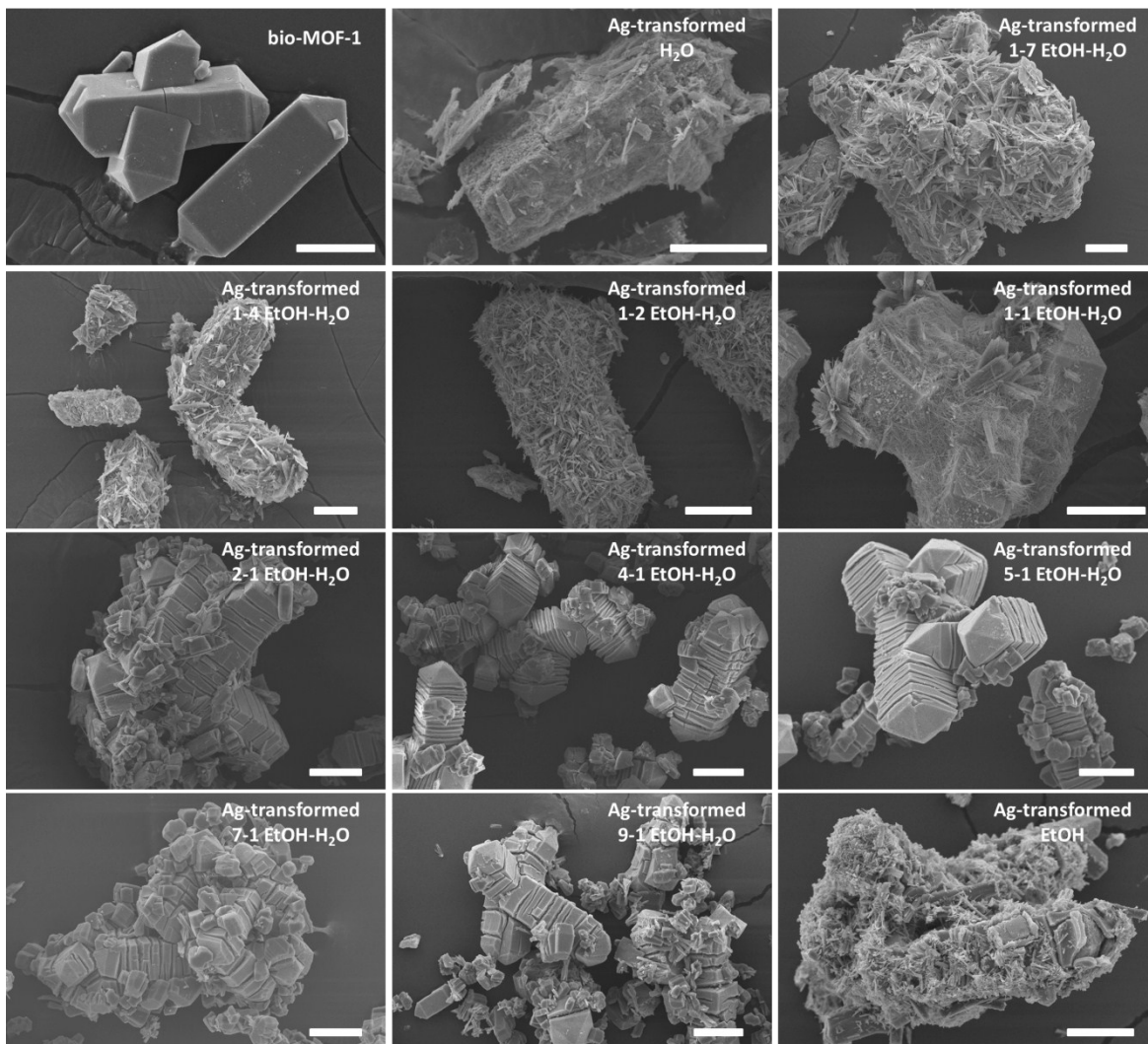


Figure S.8: SEM pictures of pristine bio-MOF-1 and Ag-transformed samples from various EtOH-H₂O mixtures (Scale bar 20 μm)

The morphology changes of bio-MOF-1 are quite dependent on the different used solvents ratios. Using pure water, the original crystals of bio-MOF-1 are completely covered with small needle- and sheet-like structures, which presumably are a mixture of the 4,4'-BPDA linker and adenine precipitation after exposure to silver ions, Figure S.7. However upon silver loading from the 2-1, 4-1 or 5-1 EtOH-H₂O mixture, the parent crystals of bio-MOF-1 are still very much recognizable, although they have been fractured by stress in the material due to adenine leaching from the structure by silver complexation. For silver loading from the 9-1 EtOH-H₂O solution, the same is visible although there are again many more (larger) needle-like crystals covering the material, see Figure S.7.

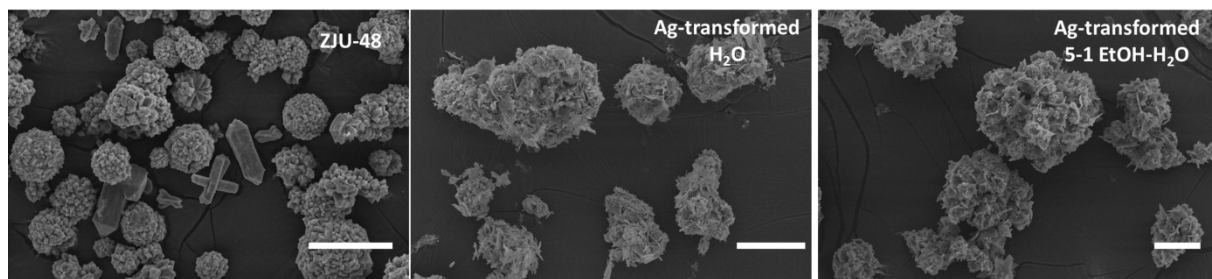


Figure S.9: SEM pictures of pristine ZJU-48 and tested Ag-transformed samples. (Scale bar: 50 μm)

ZJU-48 also crystallizes as tetragonal crystals (space group $P4/n$) but these are in contrast to bio-MOF-1 very much intergrown. Here almost no single crystals are observed and the intergrown crystallites form spherical aggregates of approximately 20 μm in diameter, see Figure S.8. Upon silver loading from either solvent mixture (H_2O or 5-1 EtOH- H_2O), the crystal morphology is retained, but again covered with very small needle-like crystals.

10. Diffuse reflectance spectra of bio-MOF-1 and ZJU-48, before and after exposure to silver

When looking at the UV absorption behaviour of these powders with diffuse reflectance spectroscopy (DRS) it is clear that the pristine bio-MOF-1 has two absorption features, both attributable to one of the organic linkers that make up the structure, being respectively adenine with an absorption maximum at 260 nm and 4,4'-BPDA with a maximum absorption at 325 nm.

Performing the silver-induced transformation of bio-MOF-1 from various ethanol-water mixtures to MOF-69A, the absorption feature of adenine seems to diminish while the absorption feature above 300 nm is broadened and blue-shifted towards 350-370 nm compared to the pristine bio-MOF-1, see Figure S.9a. This blue-shift is attributable to the presence of silver ions and silver clusters and caused by the luminescence of 4,4'-BDPA taking over. DRS also proves that both absorption features remain present in the structures and thus adenine is not completely leached out, as is expected since silver-adenine does not dissolve completely in these solvent mixtures and based on ¹H-NMR and TGA experiments. Note that the high reflectance signals (Figure S.9b) in deep UV for 4,4'-BPDA is an artefact attributed to the strong luminescence at these wavelengths which is not rejected before the detector (Figure S.10a). This caused the reflectance to be above 100% for several samples due to background luminescence, causing the Kubelka-Munk absorption to be unclear and low.

For ZJU-48 and derived silver-loaded samples, the absorption features do not change dramatically. also Note that the absorbance of the parent material is red-shifted due to the larger conjugated system of the 4,4'-*trans*-SBDA linker. Adenine absorbs at similar wavelengths compared to adenine in bio-MOF-1 (250 nm) and the 4,4'-*trans*-SBDA linker in ZJU-48 absorbs light at longer wavelengths, viz. 300-400 nm. These experiments also show that 4,4'-*trans*-SBDA absorbs stronger in the UV region 330-400 nm compared to 4,4'-BPDA. Upon silver loading, the DRS spectra remain similar which proves that adenine is not lost in this system (see also FT-IR signals similarity with pure adenine), but the mentioned red-shift of the absorption also occurs upon silver loading of this material, see Figure S.9c,d.

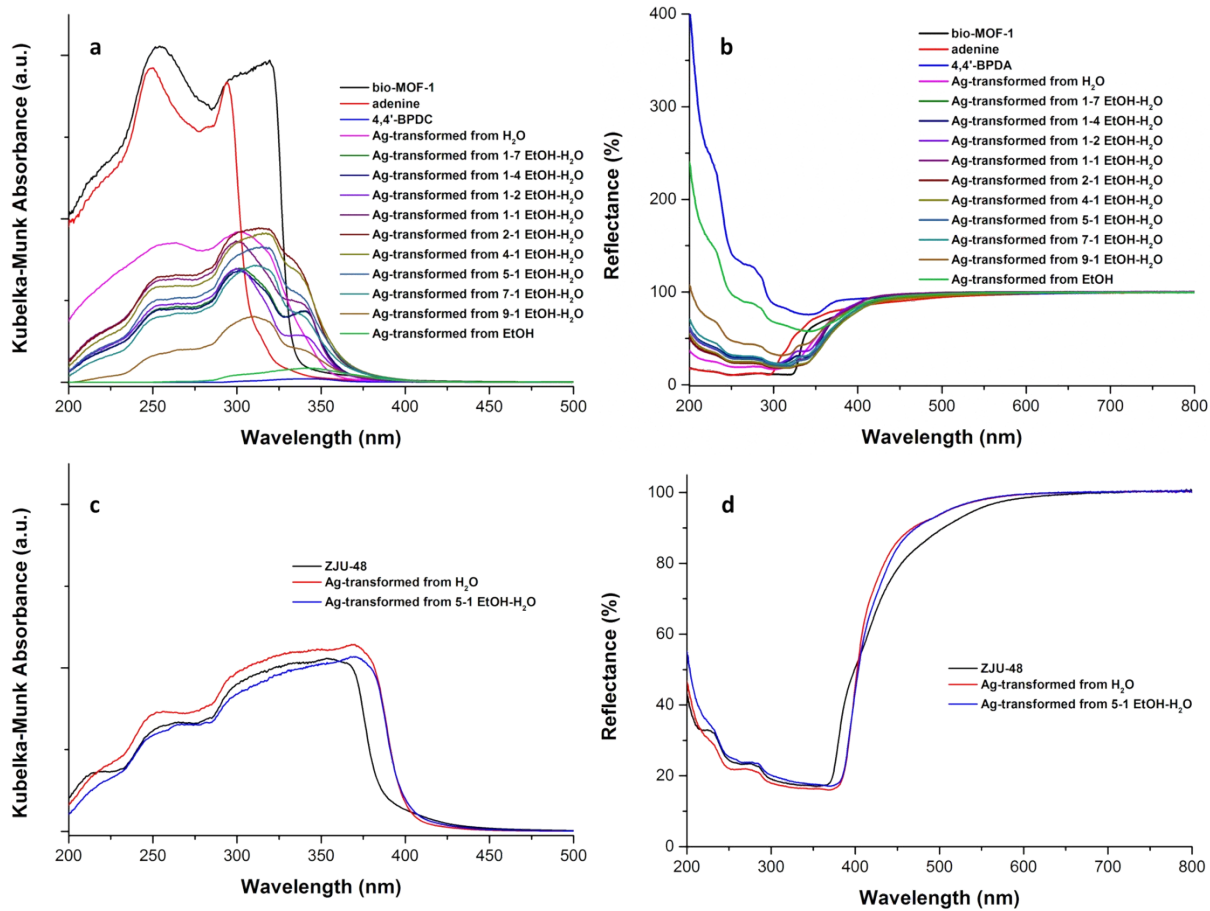


Figure S.10: Kubelka-Munk absorption of bio-MOF-1 (A) and ZJU-48 series (C) and corresponding full DRS curves (B and D).

11. 2D excitation-emission plots of used linkers and bio-MOF-1 and ZJU-48

When looking at the pure linkers (Figure S.10), both carboxylates absorb over almost the whole measured UV-region (250-360 nm for 4,4'-BPDA and 250-420 nm for 4,4'-*trans*-SBDA) and their emission is equally intense over the entire excitation range, with emission at 405 nm for 4,4'-BPDA and 465 nm for 4,4'-*trans*-SBDA. After incorporation in the structure of the respective MOFs, the emission of 4,4'-BPDA remains at the same wavelengths but in contrast the emission of 4,4'-*trans*-SBDA in ZJU-48 is slightly more blue-shifted to 440 nm. In contrast, adenine absorbs only in the 350-450 nm region, giving only very weak emission that span from blue to green light (400-550 nm) upon different excitation wavelengths (Figure S.10).

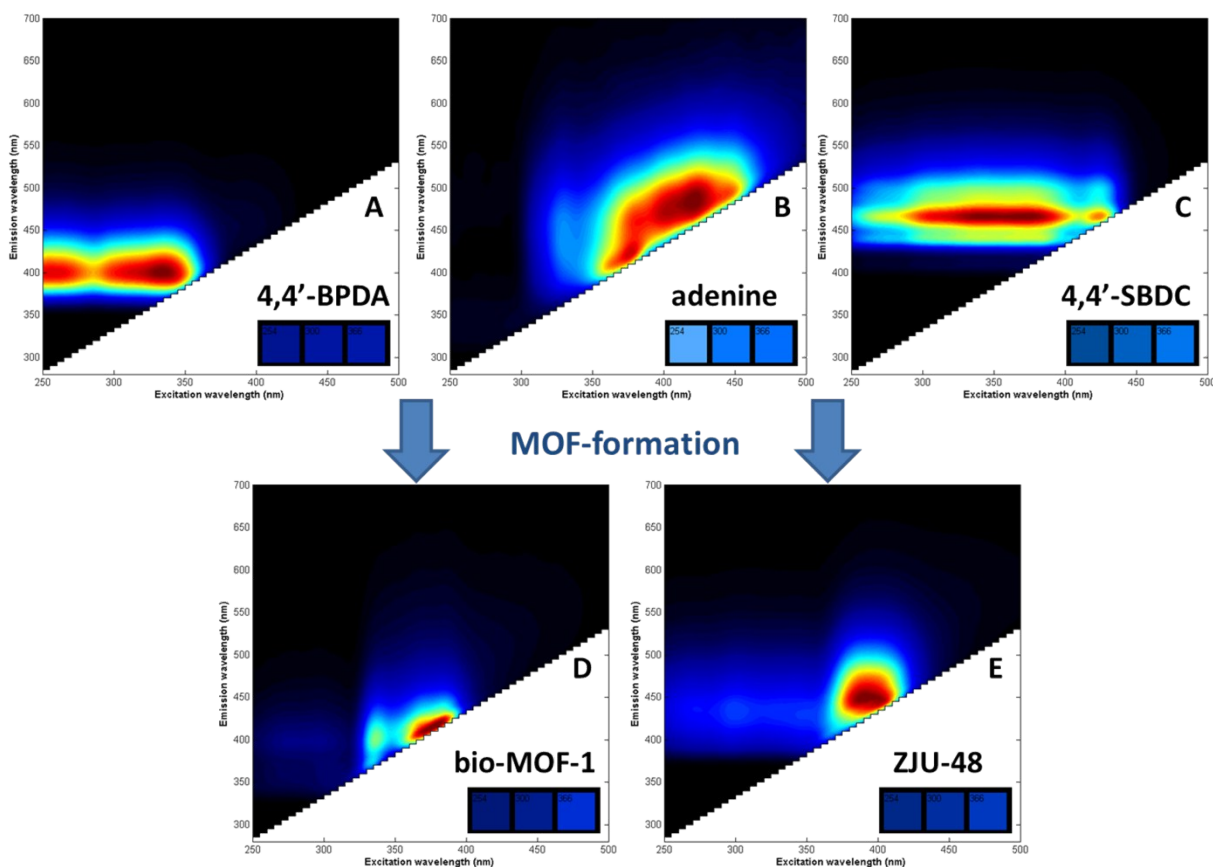


Figure S.11: Luminescence plots for powders of 4,4'-BPDA (A), adenine (B), 4,4'-*trans*-SBDA (C), bio-MOF-1 (D) and ZJU-48 (E).

12. 2D excitation-emission plots of bio-MOF-1 transformed by Ag⁺ to MOF-69A in various EtOH-H₂O solvent ratios

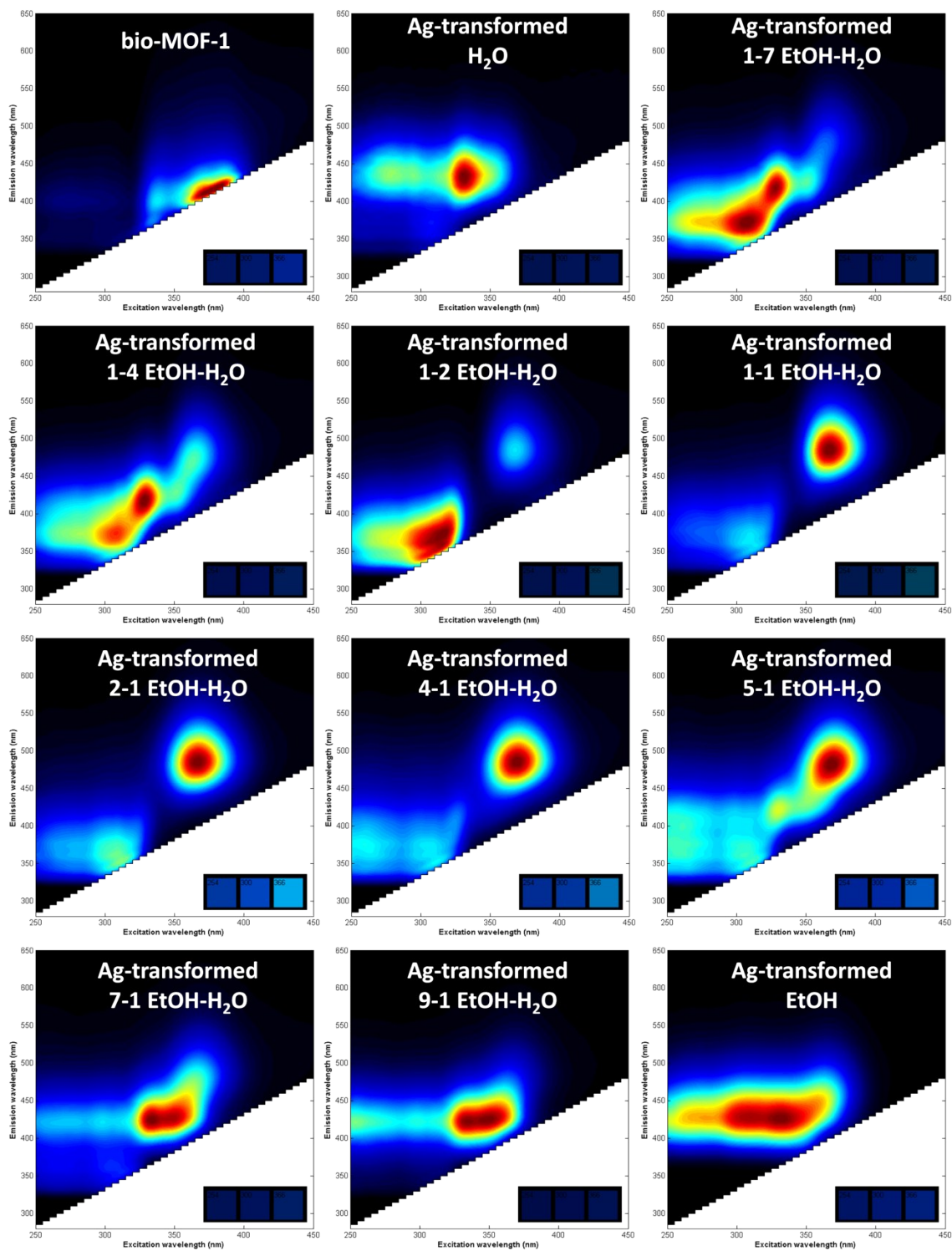


Figure S.12: 2D Excitation-emission profiles of bio-MOF-1 and the same material exposed to Ag⁺ in EtOH-H₂O solutions.

13. Comparison of spectral features of Ag-transformed MOF to Ag-zeolites

Based on previous research in our group on luminescent silver clusters in zeolites, the shape and spectroscopic features of the silver clusters in MOFs look similar to the spectroscopic properties of silver clusters in zeolites. Because of this and since the luminescence is unlikely originating from the original framework or its consisting pure ligands, the new luminescent features in the Ag-transformed MOF samples are likely attributed to silver clusters rather than a silver complex. Figure S.13 shows a comparison between 2D-excitation/emission plots of an LTA(Li)-Ag₉ sample (a) from previous work^{14c} in our group and the most luminescent Ag-transformed MOF (from 4-1 EtOH-H₂O) presented in this work (b).

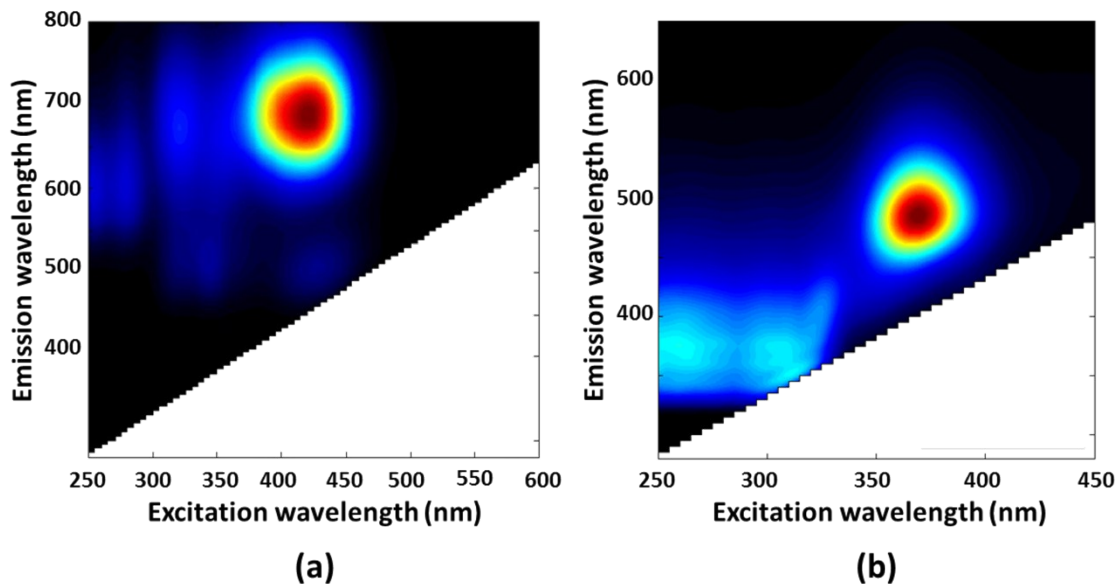


Figure S.13: Comparison of the spectral similarities between LTA(Li)-Ag₉ from our previous work (a) and the most luminescent Ag-transformed MOF sample from 4-1 EtOH-H₂O in this work (b).

14. Photographs of bio-MOF-1 before and after silver-induced transformation

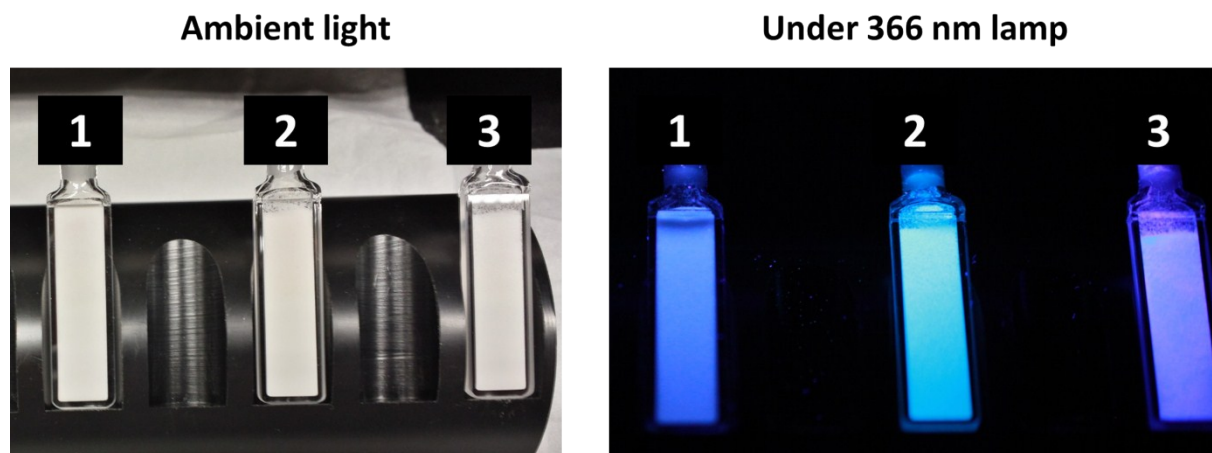


Figure S.14: Photographs of bio-MOF-1 before and after silver-induced transformation under ambient light and under a standard laboratory UV lamp ($\lambda_{ex.} = 366 \text{ nm}$) 1) bio-MOF-1 2) Ag-transformed from 4-1 EtOH-H₂O 3) Ag-transformed from 9-1 EtOH-H₂O

15. Time-resolved luminescence characterization of bio-MOF-1 and Ag-transformed to MOF-69A

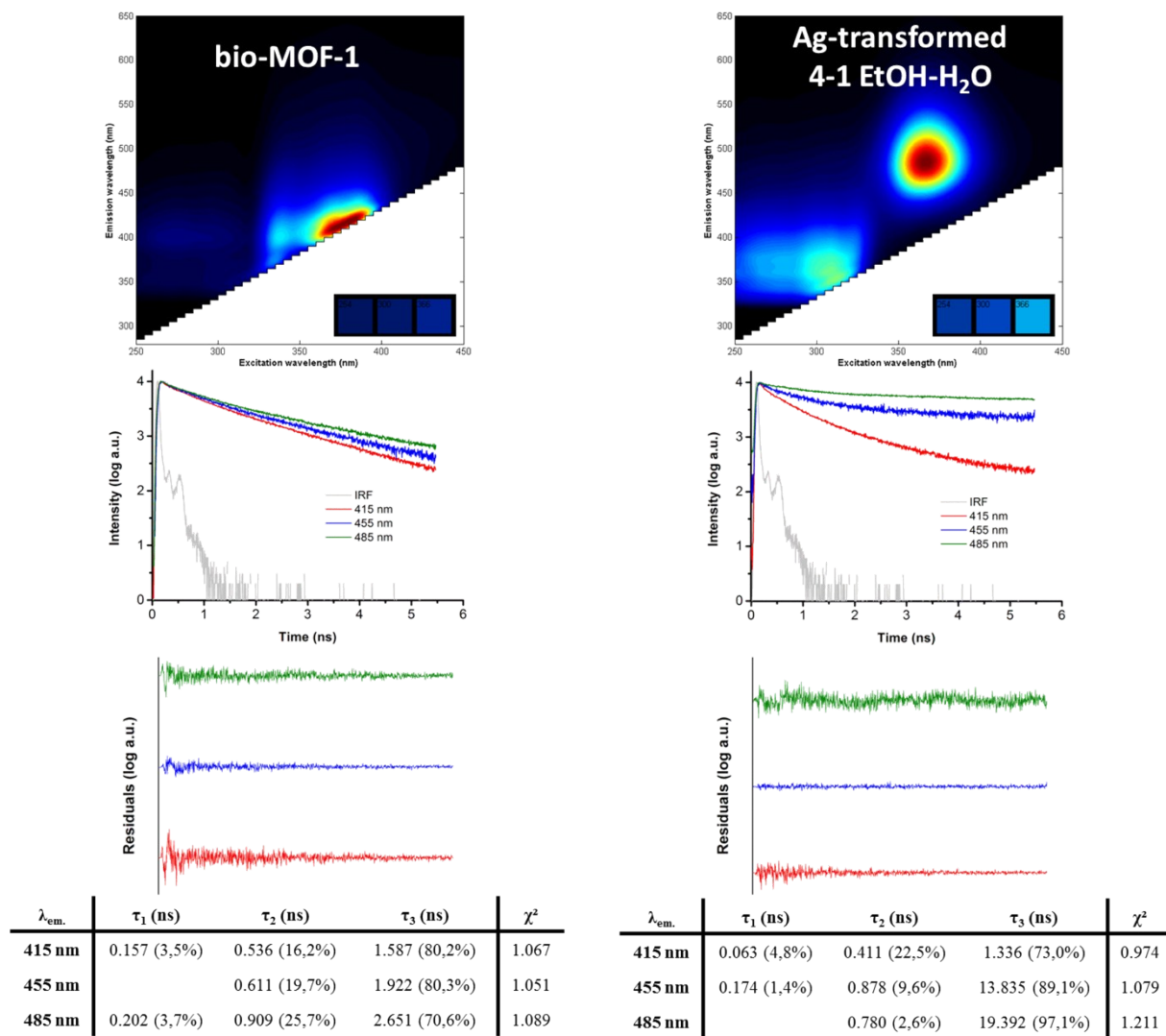


Figure S.15: Steady-state and Time-resolved luminescence characterization of bio-MOF-1 before and after Ag-induced transformation to MOF-69A

References

1. J. H. Cavka, S. Jakobsen, U. Olsbye, N. Guillou, C. Lamberti, S. Bordiga and K. P. Lillerud, *J. Am. Chem. Soc.*, 2008, **130**, 13850-13851.
2. H. Furukawa, F. Gándara, Y.-B. Zhang, J. Jiang, W. L. Queen, M. R. Hudson and O. M. Yaghi, *J. Am. Chem. Soc.*, 2014, **136**, 4369-4381.
3. B. Van de Voorde, D. Damasceno Borges, F. Vermoortele, R. Wouters, B. Bozbiyik, J. Denayer, F. Taulelle, C. Martineau, C. Serre, G. Maurin and D. De Vos, *Chemsuschem*, 2015, **8**, 3159-3166.
4. T. Loiseau, C. Serre, C. Huguenard, G. Fink, F. Taulelle, M. Henry, T. Bataille and G. Férey, *Chem. Eur. J.*, 2004, **10**, 1373-1382.
5. C. Volkringer, M. Meddouri, T. Loiseau, N. Guillou, J. Marrot, G. Férey, M. Haouas, F. Taulelle, N. Audebrand and M. Latroche, *Inorg. Chem.*, 2008, **47**, 11892-11901.
6. M. Sindoro, A.-Y. Jee and S. Granick, *Chem. Commun.*, 2013, **49**, 9576-9578.
7. J. Cravillon, C. A. Schröder, R. Nayuk, J. Gummel, K. Huber and M. Wiebcke, *Angew. Chem. Int. Ed.*, 2011, **50**, 8067-8071.
8. J. An, S. J. Geib and N. L. Rosi, *J Am Chem Soc*, 2009, **131**, 8376-8377.
9. H. Xu, J. Cai, S. Xiang, Z. Zhang, C. Wu, X. Rao, Y. Cui, Y. Yang, R. Krishna, B. Chen and G. Qian, *J. Mater. Chem.*, 2013, **1**, 9916-9921.
10. R. J. T. Houk, B. W. Jacobs, F. E. Gabaly, N. N. Chang, A. A. Talin, D. D. Graham, S. D. House, I. M. Robertson and M. D. Allendorf, *Nano Lett.*, 2009, **9**, 3413-3418.
11. E. Coutino-Gonzalez, M. B. J. Roeffaers, B. Dieu, G. De Cremer, S. Leyre, P. Hanselaer, W. Fyen, B. Sels and J. Hofkens, *J. Phys. Chem. C.*, 2013, **117**, 6998-7004.
12. G. De Cremer, Y. Antoku, M. B. J. Roeffaers, M. Sliwa, J. Van Noyen, S. Smout, J. Hofkens, D. E. De Vos, B. F. Sels and T. Vosch, *Angew. Chem. Int. Ed.*, 2008, **47**, 2813-2816.
13. D. Loos, M. Cotlet, F. De Schryver, S. Habuchi and J. Hofkens, *Biophys. J.*, 2004, **87**, 2598-2608.
14. (a) E. Coutino-Gonzalez, D. Grandjean, M. Roeffaers, K. Kvashnina, E. Fron, B. Dieu, G. De Cremer, P. Lievens, B. Sels and J. Hofkens, *Chem. Commun.*, 2014, **50**, 1350-1352; (b) G. De Cremer, E. Coutino-Gonzalez, M. B. Roeffaers, B. Moens, J. Ollevier, M. Van der Auweraer, R. Schoonheydt, P. A. Jacobs, F. C. De Schryver, J. Hofkens, D. E. De Vos, B. F. Sels and T. Vosch, *J Am Chem Soc*, 2009, **131**, 3049-3056.1. (c) E. Coutino-Gonzalez, W. Baekelant, D. Grandjean, M. B. J. Roeffaers, E. Fron, M. S. Aghakhani, N. Bovet, M. Van der Auweraer, P. Lievens, T. Vosch, B. Sels and J. Hofkens, *J. Mat. Chem. C*, 2015, **3**, 11857-11867.